



Virology | Full-Length Text

Pathogenicity and landscape of differential gene expression in mice orally infected with clinical coxsackievirus A6 (CA6)

Lihong Zhang,^{1,2,3} Wanjun Peng,^{1,2,3} Jing Wu,^{1,2,3} Xiaohui Wei,^{1,2,3} Na Rong,^{1,2,3} Gengxin Zhang,^{1,2,3} Hekai Yang,^{1,2,3} Xiaoyue Ding,⁴ Binbin Zhao,^{1,2,3} Jiangning Liu^{1,2,3}

AUTHOR AFFILIATIONS See affiliation list on p. 17.

ABSTRACT Hand, foot, and mouth disease (HFMD) is caused by more than 20 pathogenic enteroviruses belonging to the Picornaviridae family and *Enterovirus* genus. Since the introduction of the enterovirus-71 (EV71) vaccine in 2016, the number of HFMD cases caused by EV71 has decreased. However, cases of infections caused by other enteroviruses, such as coxsackievirus A6 (CA6) and coxsackievirus A10, have been increasing accordingly. In this study, we used a clinical isolate of CA6 to establish an intragastric infection mouse model using 7-day-old mice to mimic the natural transmission route, by which we investigated the differential gene expression profiles associated with virus infection and pathogenicity. After intragastric infection, mice exhibited hind limb paralysis symptoms and weight loss, similar to those reported for EV71 infection in mice. The skeletal muscle was identified as the main site of virus replication, with a peak viral load reaching 2.31×10^7 copies/mg at 5 dpi and increased infiltration of inflammatory cells. RNA sequencing analysis identified differentially expressed genes (DEGs) after CA6 infection. DEGs in the blood, muscle, brain, spleen, and thymus were predominantly enriched in immune system responses, including pathways such as Toll-like receptor signaling and PI3K-Akt signaling. Our study has unveiled the genes involved in the host immune response during CA6 infection, thereby enhancing our comprehension of the pathological mechanism of HFMD.

IMPORTANCE This study holds great significance for the field of hand, foot, and mouth disease (HFMD). It not only delves into the disease's etiology, transmission pathways, and severe complications but also establishes a novel mouse model that mimics the natural coxsackievirus A6 infection process, providing a pivotal platform to delve deeper into virus replication and pathogenic mechanisms. Additionally, utilizing RNA-seq technology, it unveils the dynamic gene expression changes during infection, offering valuable leads for identifying novel therapeutic drug targets. This research has the potential to enhance our understanding of HFMD, offering fresh perspectives for disease prevention and treatment and positively impacting children's health worldwide.

KEYWORDS hand, foot, and mouth disease (HFMD), coxsackievirus A6 (CA6), mouse model, RNA-seq

Hand, foot, and mouth disease (HFMD) is a common infectious disease that primarily affects children younger than age 5. According to the World Health Organization, millions of people worldwide are infected with HFMD-causing pathogens each year, with most cases occurring in children. HFMD typically presents as a mild self-limiting illness characterized by fever, vesicular rash on the hands, feet, and buttocks, and oral mucosal ulcers. However, some patients may develop severe complications, such as meningitis, encephalitis, acute flaccid paralysis, and neurorespiratory syndrome (1, 2). HFMD was first reported in New Zealand in 1957 and has since caused outbreaks in

Editor Christiane E. Wobus, University of Michigan Medical School, Ann Arbor, Michigan, USA

Address correspondence to Jiangning Liu, liujn@cnlas.org, or Binbin Zhao, zhaocaomei@163.com.

The authors declare no conflict of interest.

See the funding table on p. 18.

Received 8 September 2023

Accepted 15 December 2023

Published 16 January 2024

Copyright © 2024 American Society for Microbiology. All Rights Reserved.

various countries and regions. The main causative agents of HFMD are enteroviruses (3), including enterovirus-71 (EV71) and coxsackievirus A16 (CA16) (4). CA16 was the predominant HFMD-causing virus during the 1970s to 1980s, but in the 1990s, EV71 gradually replaced CA16 and became the dominant HFMD-causing virus (5). Since the introduction of the EV71 vaccine in 2016, the number of HFMD cases caused by EV71 have decreased correspondingly. However, there has been an increase in cases caused by other enteroviruses, such as CA6, CA10, particularly in India, Southeast Asia, and Europe. Additionally, the incidence of neurological complications and mortality rates associated with these viruses has also increased (5, 6).

Previous studies have demonstrated a significant rise in the number of HFMD cases attributed to non-EV71 and non-CA16 viruses, with cases related to CA6 infection being particularly prominent (7, 8). To date, three countries in the European region of the World Health Organization have reported outbreaks of HFMD associated with CA6: Finland (9, 10), France (11), and Spain (12). However, large-scale outbreaks have also been reported in Asia (12, 13) and the United States (13, 14). In addition to its neurological impact, CA6 infection is characterized by extensive and severe rashes, exhibiting atypical distribution patterns including the limbs and trunk (15). Skin peeling and nail shedding are also common manifestations (16). Recent research has elucidated the potential for severe complications resulting from CA6 infection, including aseptic meningitis, brainstem encephalitis (BE), acute flaccid paralysis, and even potential pulmonary edema (9, 17, 18).

Several animal models for CA6 infection have been developed to study the pathogenesis of HFMD caused by CA6, including intraperitoneal infection of 1-day-old BALB/c mice (19), intramuscular injection of 5-day-old ICR mice (20), and intraperitoneal inoculation of 10-day-old BALB/c mice (21). Ten-day-old ICR mice were subjected to intraperitoneal injection and oral administration for infection (22). However, a novel mouse model orally infected with CA6 to simulate the natural infection route is necessary to characterize the replication and pathogenicity of CA6 without bias. In addition, to deeply reveal the dynamic landscape of gene expression involved in CA6 infection, which is thought to be valuable for understanding the pathogenicity of CA6 infection and to screen potential drug targets for treatment, we performed RNA-seq to investigate the alterations in gene expression in different tissues of CA6-infected mice.

RESULTS

The replication of CA6 virus in tissues of mice after intragastric infection

To assess the virulence of the clinically isolated CA6 strain, 7-day-old BALB/c mice were infected via intragastric administration of a viral inoculum of $1 \times 10^{6.5}$ TCID₅₀ per mouse. The mice exhibited fur, diarrhea, and hind limb paralysis starting on the fourth day post infection (4 dpi) (Fig. 1A) and demonstrated a trend of halted growth in terms of body weight (Fig. 1B). Intragastric infection led to the death of all mice within 8 days post-infection (Fig. 1C).

After infection, the viral loads in the blood and main tissues were quantified using fluorescence-based real-time PCR. At 3 dpi, the viral load in the blood reached its peak (2.57×10^5 copies/ μ L) (Fig. 1D), while the viral load in muscle tissue peaked at 2.31×10^7 copies/mg at 5 dpi (Fig. 1E) and remained high thereafter. From 1 to 3 dpi, the enhancement of viral load was detected in nearly all the checked tissues, which suggested potential virus replication or spread of virus from viremia (Fig. 1D through N). At 3 dpi, the viral load in the heart, lung, liver, and stomach of infected mice exceeded 10^4 copies/mg, and the viral load in the brain and large intestine increased from 3 to 5 dpi. Notably, an obvious decline in viral load was detected in the heart and liver from 5 to 7 dpi (Fig. 1F and H). Interestingly, the viral load of the spinal cord continued to increase at least before 7 dpi and reached 1.79×10^5 copies/mg (Fig. 1N), and these results indicated a delay in viral invasion and replication in neurological tissues compared to other tissues. In contrast, merely lower viral loads were detected at 5 and 7 dpi in the thymus and spleen (Fig. 1O and P). Compared to other tissues, the highest viral load was detected in

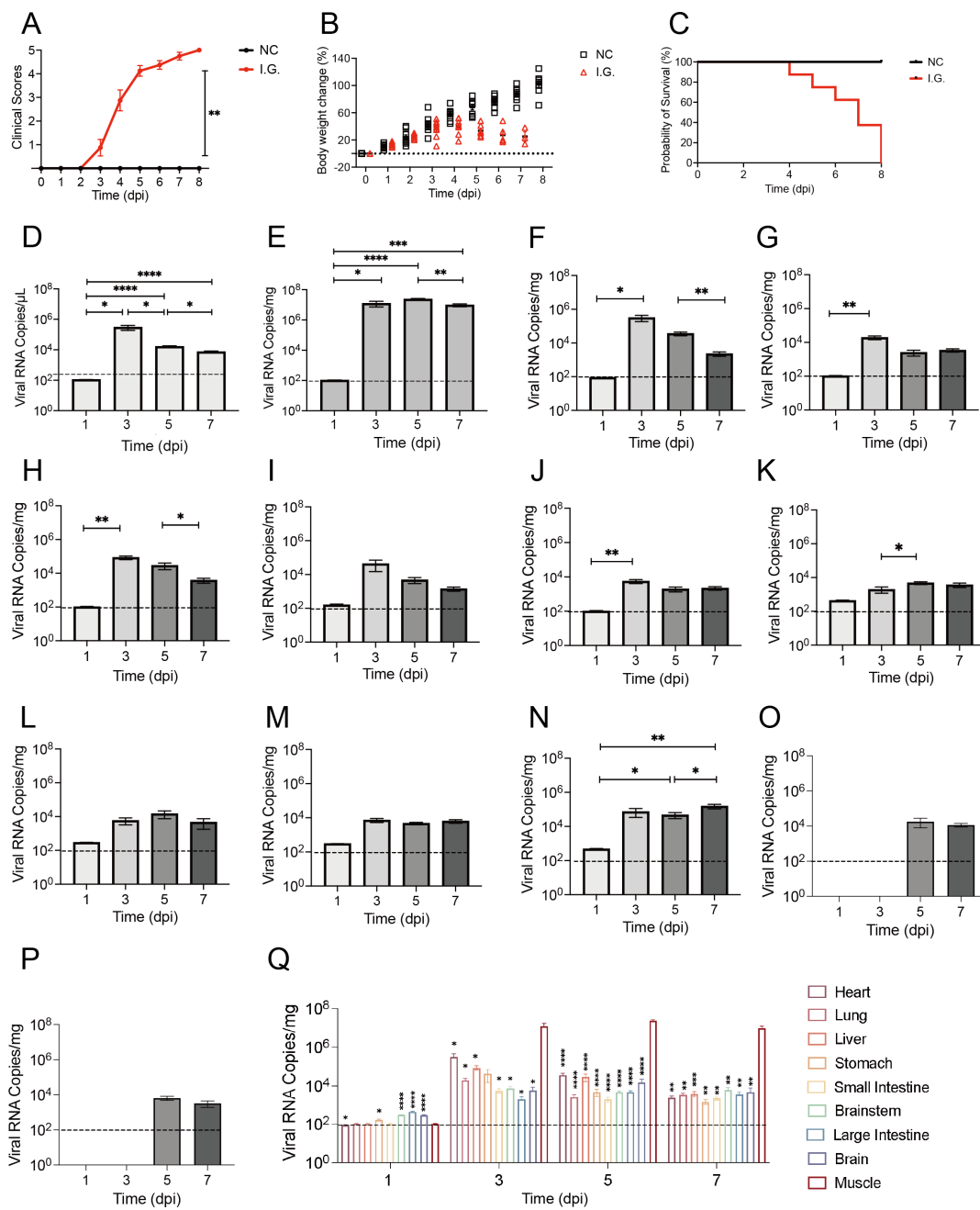


FIG 1 Clinical data of CA6-infected mice via intragastric gavage. (A) Clinical scores. (B) Body weight changes. (C) Survival rates. Viral load at different tissues was determined by qRT-PCR at 1, 3, 5, and 7 dpi, respectively (D–Q). (D) Blood. (E) Skeletal muscle. (F) Heart. (G) Lung. (H) Liver. (I) Stomach. (J) Small intestine. (K) Large intestine. (L) Brain. (M) Brain stem. (N) Spinal cord. (O) Thymus. (P) Spleen. (Q) Comparison on the viral loads of each tissue to skeletal muscle at each timepoints, and * represents a significant difference in viral load of each tissue compared to muscle. Error bars show the SEM. $n = 6$ at each timepoint. *, $P < 0.05$; **, $P < 0.01$; ***, $P < 0.001$; ****, $P < 0.0001$. The dashed line represents the detection limit. Clinical scores were determined as follows: 0, healthy; 1, ruffled fur and hunchback appearance; 2, wasting and limb weakness; 3, single limb paralysis; 4, paralysis of both limbs; 5, moribund and death.

skeletal muscle (Fig. 1Q), which indicated that the CA6 virus demonstrated tropism for muscle cells similar to EV71 and CA16.

Inflammatory cell proliferation and infiltration

Both immunohistochemistry and immunofluorescence demonstrated abundant accumulation of neutrophils and macrophages in muscle beginning at 3 dpi. However,

in contrast to muscle, only neutrophils were observed in the spinal cord at a later stage after infection, as nearly no macrophages were detected, which suggested that CA6 infection specifically induced neutrophil infiltration in the spinal cord (Fig. 2). The proliferation of both neutrophils and monocytes was detected by flow cytometry in peripheral blood after infection, and the counts and proportions of neutrophils peaked at 5 dpi, and neutrophils accounted for a high proportion of 60% of the total white blood cells. Compared to the mice of negative control and 1 dpi, the proportions of monocyte decreased at 5 dpi (Fig. 3).

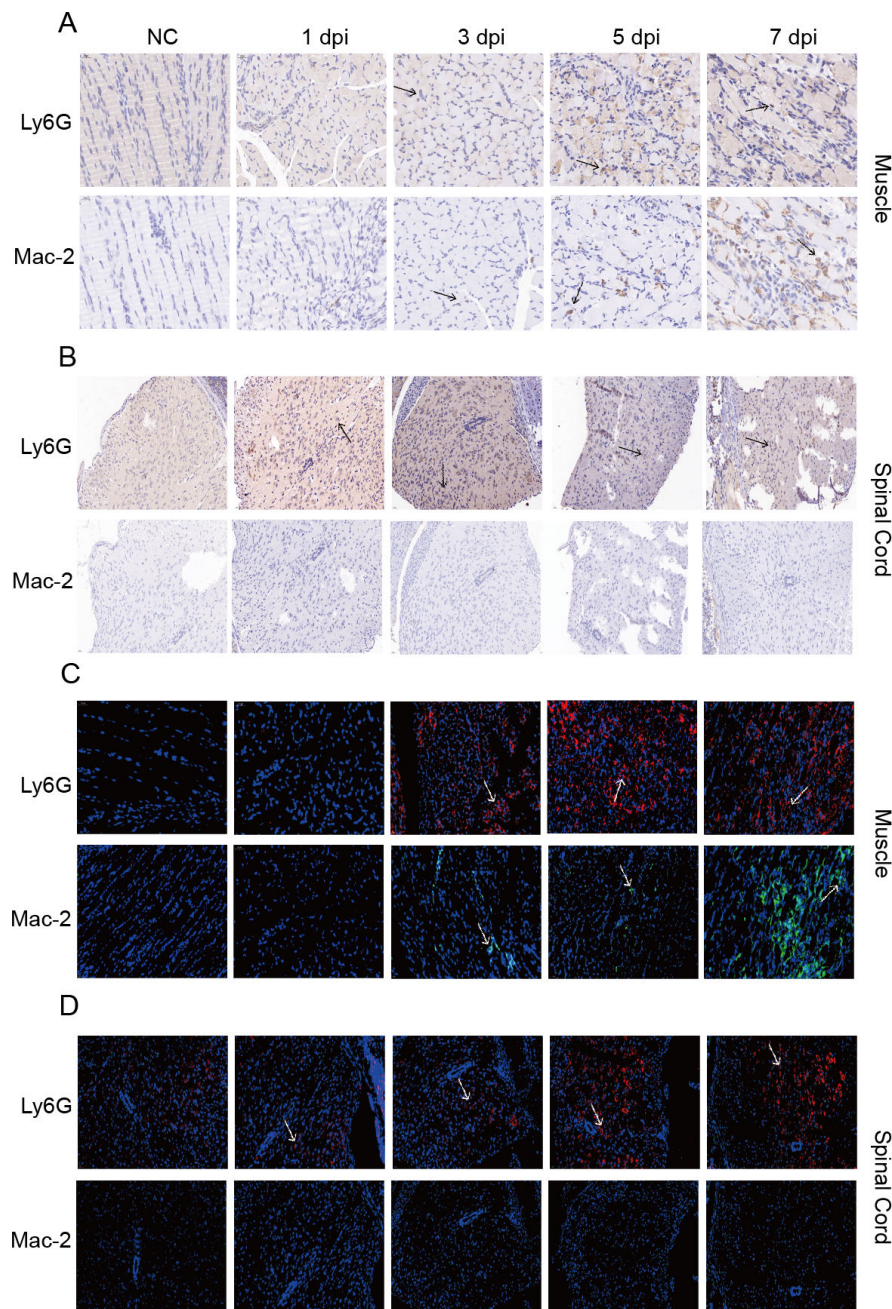


FIG 2 Immunohistochemistry and immunofluorescence detected the distribution of neutrophils and macrophages in muscle and spinal cord of infected mice. Immunohistochemistry of muscle (A) and spinal cord (B). Immunofluorescence of muscle (C) and spinal cord (D). The typical results of three sections of each mouse at each timepoints ($n = 6$) were representatively shown. 200 \times . The arrows represent typical lesion sites.

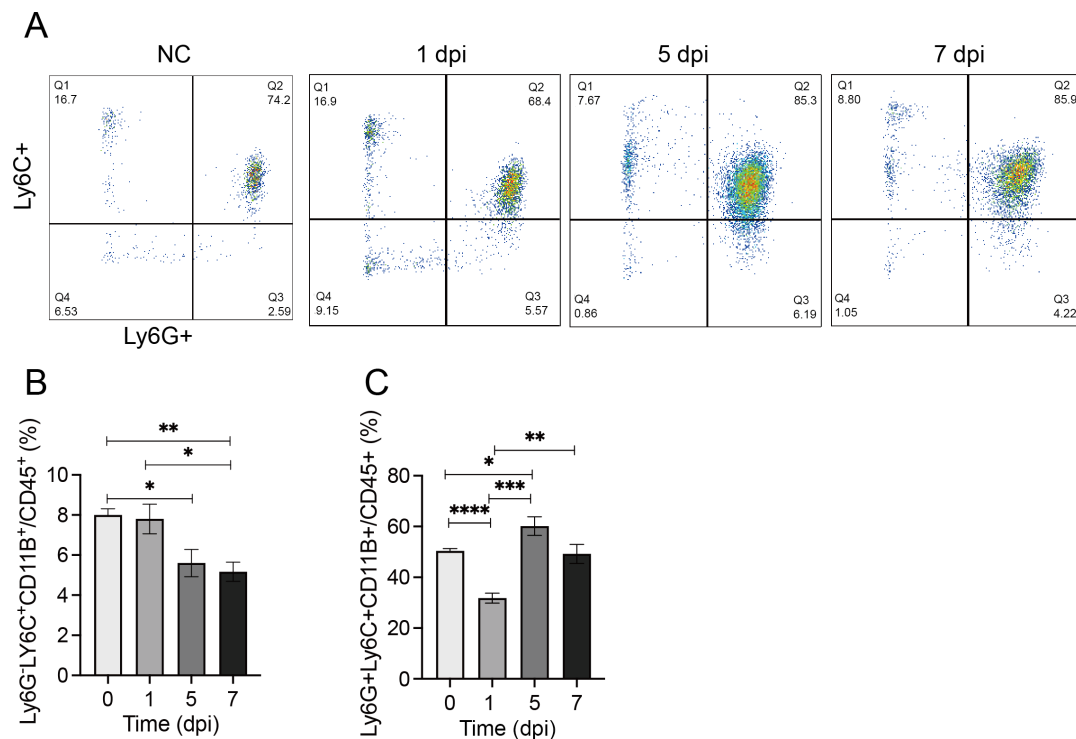


FIG 3 Fluctuations of neutrophils and monocytes in peripheral blood of mice after CA6 infection. Typical FCS results were represented (A), and statistical charts for monocytes (B) and neutrophils (C) were shown. Error bars show the SEM. $n = 6$ at each timepoints. *, $P < 0.05$; **, $P < 0.01$; ***, $P < 0.001$; ****, $P < 0.0001$.

Landscape of inflammatory cytokines and gene expression profiles of blood

Elevated secretion of CXCL1, IL-1 α , IL-2, IL-23, and IL-6 was detected and peaked at either 3 or 5 dpi. In addition, IFN- γ , IL-12p70, IL-18, and TNF- α demonstrated persistent increases in expression from 3 to 7 dpi (Fig. 4A). This result indicated that CA6 infection elicited an intensive proinflammatory response in mice.

To reveal the genes associated with CA6 infection, a differential gene expression analysis followed by GO and KEGG analysis was performed in blood, muscle, brain, thymus, and spleen at 3, 5, and 7 dpi.

A total of 1,399 genes were found to be commonly differentially expressed at different timepoints in blood compared to the noninfected control group (Fig. 4B). GO and KEGG analyses revealed that the differentially expressed genes (DEGs) were mainly enriched in the immune system response, such as the Toll-like receptor pathway (Fig. 4C), and immune-related pathways, including the NOD-like receptor pathway and JAK-STAT signaling pathway (Fig. 4D). Among the DEGs, there were 688 upregulated genes (Fig. 4E) and 599 downregulated genes (Fig. 4F). Furthermore, the number of upregulated and downregulated genes at different timepoints were identified (Fig. S1A through C). According to GO analysis, the upregulated genes were primarily enriched in cytokine-mediated signaling pathways, cellular activation involved in the immune response, regulation of the innate immune response, and the response to viruses (Fig. S1D through F), and the downregulated genes were mainly enriched in processes related to cell development and metabolism, cellular metabolic processes, and the adaptive immune response (Fig. S1G through I). According to KEGG analysis, the upregulated genes were mainly enriched in pathways such as the NOD-like receptor signaling pathway, Toll-like receptor signaling pathway, B-cell receptor signaling pathway, and JAK-STAT signaling pathway (Fig. S1J through L), while the downregulated genes were mainly enriched in pathways related to autophagy, T-cell receptor signaling pathway, and intestinal immune network for IgA production (Fig. S1M through O). The fuzzy C-means clustering algorithm was used to screen the temporal specificity of DEGs postinfection. We combined

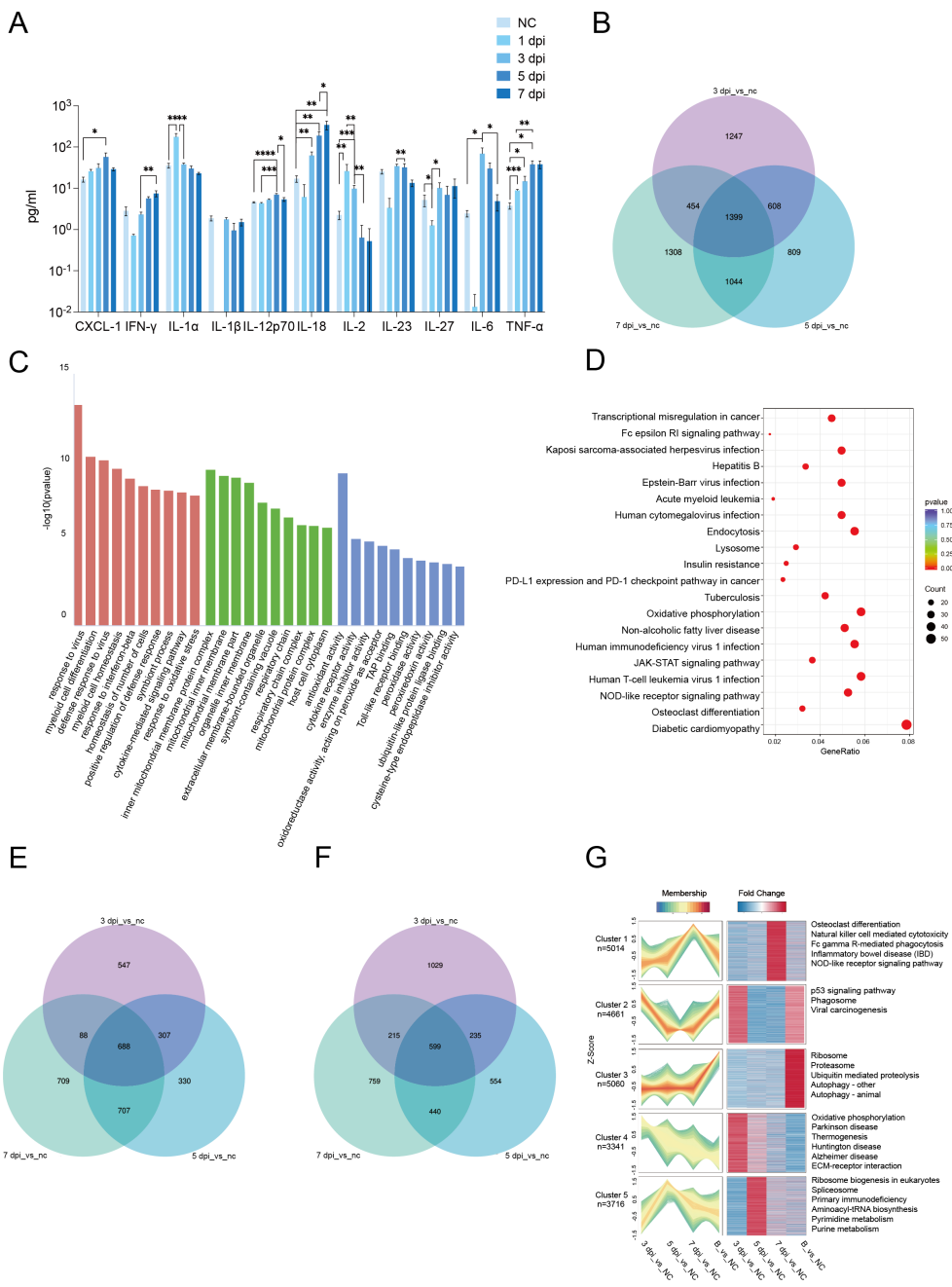


FIG 4 Changes in inflammatory factors and dynamic of gene expression profiles in peripheral blood of mice after CA6 infection. (A) Proliferation of inflammatory factors ($n = 6$). (B) Venn diagram of common differentially expressed genes (DEGs) at different timepoints. (C) GO analysis of common DEGs (B). (D) KEGG analysis of common DEGs (B). (E and F) Venn diagram of commonly upregulated (E) and downregulated (F) DEGs. (G) Fuzzy C-means clustering of DEGs in blood at 3, 5, and 7 dpi. The value of B_vs_NC is set to 1. Error bars show the SEM. *, $P < 0.05$; **, $P < 0.01$; ***, $P < 0.001$; ****, $P < 0.0001$.

the DEGs from the three timepoints into a union set and used the fuzzy C-means algorithm to classify the DEGs into five clusters based on the FC value. Clusters 1, 2, 4, and 5 represent the upregulated DEGs at three timepoints, while Cluster 3 represents the downregulated DEGs at three timepoints, including those related to autophagy (Atg9a, Cul3) (Fig. 4G). At 7 dpi, the expression of genes in the NOD-like receptor signaling pathway (Casp8, Ifi207, Ifi204), NK cell-mediated cytotoxicity (Fasl, Fcgr4, Fcer1g), and inflammatory bowel disease (IBD) (Il18r1, Il18rap, Tlr5) was upregulated (Cluster 1). At 3

dpi, the expression of genes associated with phagosomes (Marco, Rab7b) and oxidative phosphorylation (Ndufb3, Ndufs1, Atp5e) was upregulated (Clusters 2 and 4). At 5 dpi, the expression of genes belonging to metabolism (Dhodh, Polr3d, Nt5e) and immune deficiency (Cd28, Icos, Itga4) was upregulated (Cluster 5).

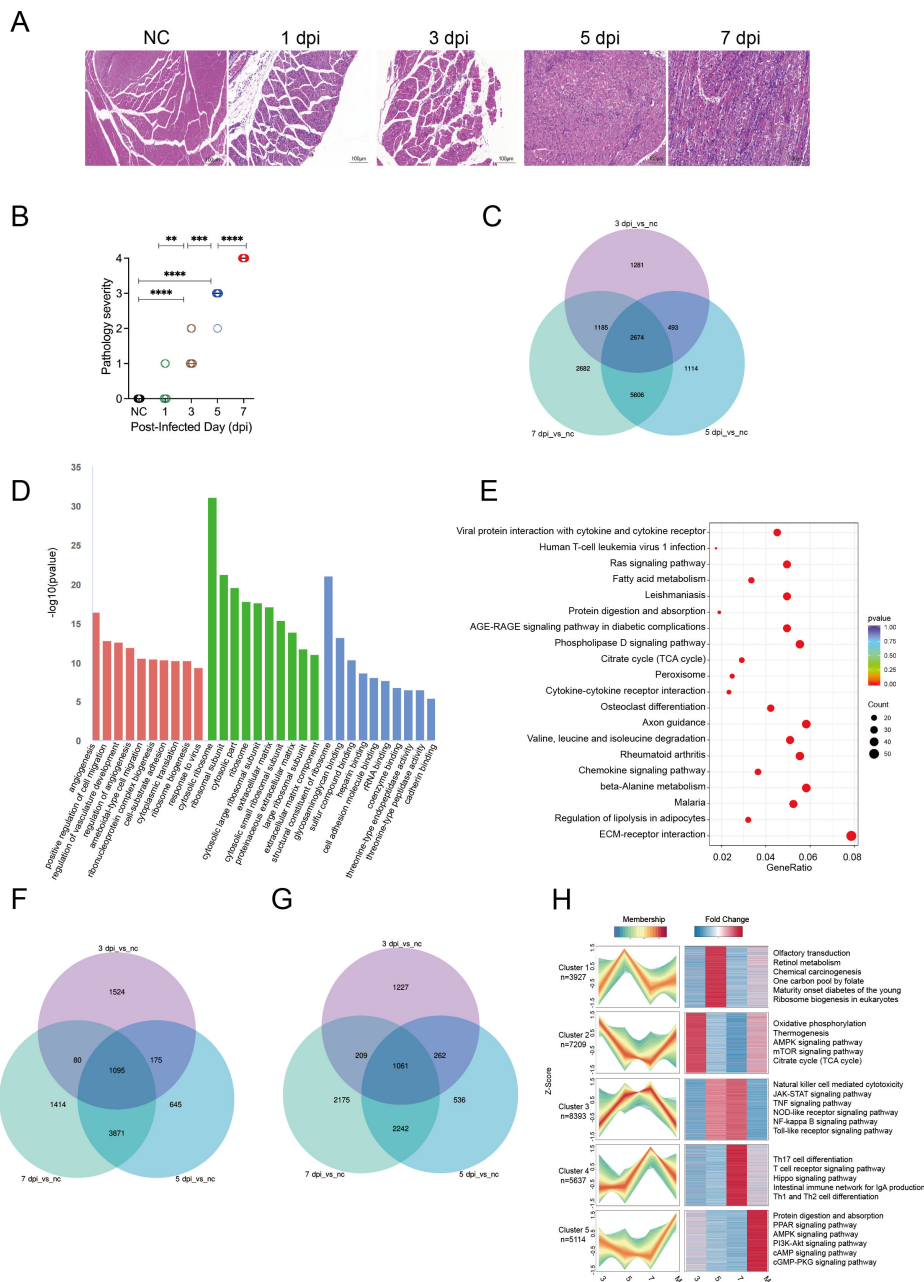


FIG 5 Pathological changes and dynamic of gene expression profiles in mouse muscles after CA6 infection. (A) Pathological changes of muscles. The arrows represent typical lesion sites, 200x. (B) Histopathological scores of muscle tissues. (C) Venn diagram of common DEGs at different timepoints. (D) GO analysis of common DEGs (C). (E) KEGG analysis of common DEGs (C). (F–G) Venn diagram of commonly upregulated (F) and downregulated (G) DEGs. (H) Fuzzy C-means clustering of muscles at 3, 5, and 7 dpi, respectively. The value of M_vs_NC is set to 1. Histopathological scores were determined as follows: 0, normal (normal muscle fibers without inflammation); 1, minimal (occasionally visible inflammatory cell infiltration); 2, mild (scattered or focal inflammatory cell infiltration); 3, moderate (diffuse inflammatory cell infiltration and mild muscle fiber degeneration or necrosis); 4, severe (severe inflammatory cell infiltration and muscle fiber degeneration and necrosis). **, P < 0.01; ***, P < 0.001; ****, P < 0.0001.

Histopathological changes and differential gene expression profiles of muscle

Histopathological examination demonstrated severe damage to the hind limb skeletal muscles in virus-infected mice, characterized by degeneration and necrosis of muscle cells and infiltration of inflammatory cells (Fig. 5A through B). A total of 2,674 genes were found to be commonly differentially expressed at different timepoints in muscle compared to the noninfected control group (Fig. 5C). GO and KEGG analyses revealed that the DEGs were mainly enriched in ribosomes and cell migration (Fig. 5D) and the Ras signaling pathway and chemokine signaling pathway (Fig. 5E). Among the DEGs, there were 1,095 upregulated genes (Fig. 5F) and 1,061 downregulated genes (Fig. 5G).

The number of upregulated or downregulated genes at different timepoints were screened (Fig. S2A through C). GO analysis indicated that the upregulated genes were mainly enriched in cellular respiration, oxidative phosphorylation, regulation of leukocyte activation, cytokine activity, leukocyte-mediated immunity, and T-cell activation, while the downregulated genes were mainly enriched in cell migration, small molecule catabolic processes, fatty acid oxidation, and ATP metabolic processes (Fig. S2D through I). KEGG analysis revealed that the upregulated genes were mainly enriched in the RIG-I-like receptor signaling pathway, Toll-like receptor signaling pathway, and NF- κ B signaling pathway, while the downregulated genes were mainly enriched in the PI3K-Akt signaling pathway, Rap1 signaling pathway, PPAR signaling pathway, AMPK signaling pathway, Wnt signaling pathway, and mTOR signaling pathway (Fig. S2J through O).

According to the fuzzy C-means clustering algorithm, Clusters 1, 2, 3, and 4 represent the upregulated DEGs at the three timepoints, while Cluster 5 represents the downregulated DEGs, such as the cAMP signaling pathway (*Creb1*, *Atp2b4*, *Atp1a4*) and PPAR signaling pathway (*Acsl3*, *Dbi*, *Rxra*) (Fig. 5H). At 5 dpi, the expression of genes involved in ribosomes (*Rpp38*, *Nop10*, *Spata5*) and retinol metabolism (*Aox3*, *Cyp4a29*, *Dhrs3*) was upregulated (Cluster 1), while the expression of genes related to oxidative phosphorylation (*Cox5b*, *Ndufb3*, *Ndufs1*) and the AMPK signaling pathway (*Stradb*, *Prkag3*, *Irs1*) was upregulated at 3 dpi (Cluster 2). Furthermore, the expression of genes associated with the JAK-STAT signaling pathway (*Stat4*, *Stat1*, *Bcl2*), TNF signaling pathway (*Cflar*, *Casp8*, *Ptgs2*), and NOD-like receptor signaling pathway (*Stat1*, *Casp8*, *Bcl2*) was persistently upregulated at 5 and 7 dpi (Cluster 3), whereas the expression of genes belonging to the T-cell receptor signaling pathway (*Zap70*, *Ctla4*, *Icos*) and the intestinal immune network for IgA production (*Icos*, *Cxcr4*, *Pigr*) was upregulated only at 7 dpi (Cluster 4).

Histopathological changes and dynamics of gene expression profiles in the brain

Following infection, the brain tissues of mice showed abundant and tightly arranged neurons with normal morphological structures, clear nuclear-cytoplasmic boundaries, and prominent nucleoli, which suggested that CA6 infection failed to cause obvious pathological changes in the brains of mice (Fig. 6A). A total of 4,251 genes were found to be commonly differentially expressed at different timepoints in the brain compared to the noninfected control group (Fig. 6B). GO and KEGG analysis revealed that the DEGs were mainly enriched in ATP metabolic process and respiratory chain (Fig. 6C) and the MAPK signaling pathway and phospholipase D signaling pathway (Fig. 6D). Among the DEGs, there were 2,026 upregulated genes (Fig. 6E) and 2,205 downregulated genes (Fig. 6F). The number of upregulated or downregulated genes in the brain at different timepoints were identified (Fig. S3A through C). According to GO analysis, the upregulated genes were mainly enriched in cell respiration, ATP metabolic process, and oxidative phosphorylation, while downregulated genes were mainly enriched in histone methylation and chromosome segregation (Fig. S3D through I). KEGG analysis revealed that the upregulated genes were mainly enriched in oxidative phosphorylation, Toll-like receptor signaling pathway, and phagocytosis, while downregulated genes were mainly

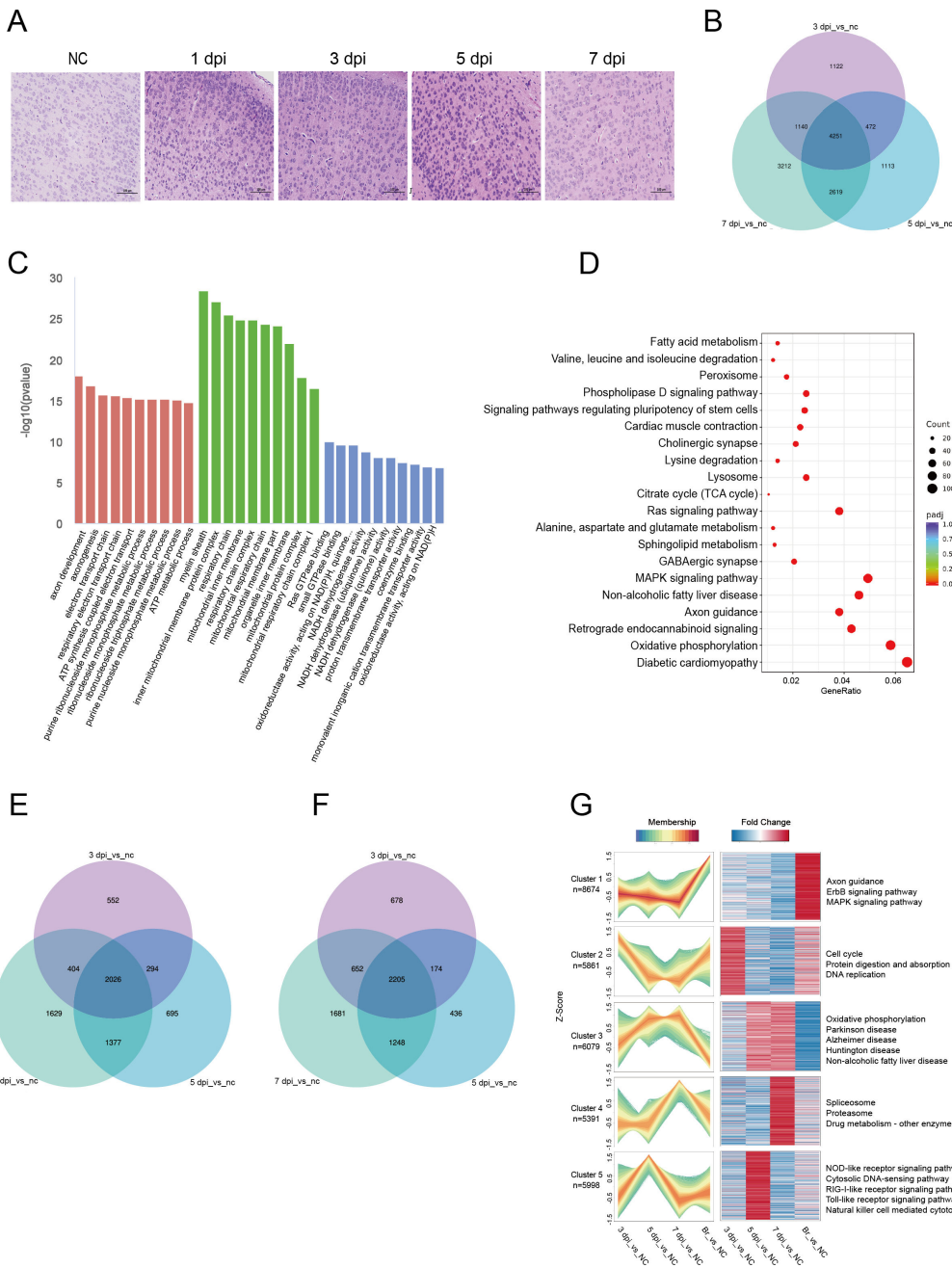


FIG 6 Pathological changes and dynamic of gene expression profiles in mouse brain after CA6 infection. (A) Pathological changes in brain. 200×. (B) Venn diagram of common DEGs at different timepoints. (C) GO analysis of common DEGs. (D) KEGG analysis of common DEGs. (E) and (F) Venn diagram of commonly upregulated (E) and downregulated (F) DEGs. (G) Fuzzy C-means clustering of brain at 3, 5, and 7 dpi, respectively. The value of Br_vs_NC is set to 1.

enriched in the PI3K-Akt signaling pathway, AMPK signaling pathway, mTOR signaling pathway, and arginine degradation (Fig. S3J through O).

According to the fuzzy C-means clustering algorithm (Fig. 6G), Clusters 2, 3, 4, and 5 represent the upregulated differentially expressed genes at three timepoints. Cluster 1 represents the downregulated DEGs at three timepoints, such as the MAPK signaling pathway (Map4k4, Erbb4, Cacna1e). The expression of genes involved in the cell cycle (Mcm3, Mcm6, Tgfb2) and DNA replication (Mcm3, Prim2, Mcm6) was upregulated at 3 dpi (Cluster 2), while the expression of Parkinson's disease-related genes (Cox5b,

Ndubf3, Ndufs1) was upregulated at 5 and 7 dpi (Cluster 3). However, at 7 dpi, only the proteasome-related genes (Psmd1, Psmb7, Psmd14) and spliceosome-related genes (Sf3b1, Snrpe, Prpf18) were upregulated (Cluster 4), while only the NOD-like receptor signaling pathway (Stat1, Casp8, Bcl2), RIG-I-like receptor signaling pathway (Casp8, Ikbke, Ifih1), and Toll-like receptor signaling pathway (Stat1, Casp8, Ikbke)-related genes were upregulated at 5 dpi (Cluster 5).

Differential gene expression profiles of the spleen and thymus

In the spleen, a total of 1,586 genes were found to be commonly differentially expressed at different timepoints in the spleen compared to the noninfected control group (Fig. 7A). GO and KEGG analyses revealed that the DEGs were mainly enriched in activation of the immune response and negative regulation of the Wnt signaling pathway (Fig. 7B) and the NF- κ B signaling pathway and PI3K-Akt signaling pathway (Fig. 7C). Among the DEGs, there were 986 upregulated genes (Fig. 7D) and 652 downregulated genes (Fig. 7E). The number of upregulated or downregulated genes in the spleen at different timepoints was identified (Fig. S4A through C). GO analysis indicated that the upregulated genes were mainly enriched in adaptive immune response, positive regulation of immune response, and activation of immune response, while the downregulated genes were enriched in vitamin binding, cell surface receptor signaling pathway, and negative regulation of Wnt signaling pathway (Fig. S4D through I). KEGG analysis revealed that the upregulated genes were mainly enriched in the NF- κ B signaling pathway, Toll-like receptor signaling pathway, and RIG-I-like receptor signaling pathway, while the downregulated genes were enriched in the phospholipase D signaling pathway, PI3K-Akt signaling pathway, and Wnt signaling pathway (Fig. S4J through O).

According to the fuzzy C-means clustering algorithm (Fig. 7F), Clusters 1, 2, 4, and 5 represent the upregulated DEGs at three timepoints, while Cluster 3 represents the downregulated DEGs at three timepoints, such as the PI3K-Akt signaling pathway (Creb1, Erbb4, Fn1) and Wnt signaling pathway (Fzd7, Wnt6, Vangl2). The expression of genes in RNA transport (Sumo1, Eif4e2, Rpp38) was upregulated at 5 dpi (Cluster 1), while that of the Toll-like receptor signaling pathway (Traf6, Lbp, Ikbkg) and NOD-like receptor (NLR) signaling pathway (Bcl2, Rnasel, Aim2) was persistently upregulated at 5 and 7 dpi (Cluster 2). In contrast, only the expression of cAMP signaling pathway (Adcy10, Atp1a4, Grin1) and MAPK signaling pathway (Cacna1s, Cacna1e, Dusp10) genes was upregulated at 7 dpi (Cluster 4) or 5 dpi (Cluster 5), respectively.

In the thymus, a total of 1,676 genes were found to be commonly differentially expressed at different timepoints in the thymus compared to the noninfected control group (Fig. 7G). GO and KEGG analyses revealed that the DEGs were mainly enriched in the cell cycle and active oxygen metabolic processes (Fig. 7H) and the MAPK signaling pathway and TNF signaling pathway (Fig. 7I). Among the DEGs, there were 702 upregulated genes (Fig. 7J) and 935 downregulated genes (Fig. 7K). The number of upregulated or downregulated genes in the thymus at different timepoints was identified (Fig. S5A through C). GO analysis indicated that the upregulated genes were mainly enriched in immune activation, metabolic processes, and calcium binding, while the downregulated genes were enriched in mRNA processing, DNA repair, and chromosome segregation (Fig. S5D through I). KEGG analysis revealed that the upregulated genes were mainly enriched in the AMPK signaling pathway, NF- κ B signaling pathway, and PPAR signaling pathway, while the downregulated genes were enriched in DNA repair, the p53 signaling pathway, and the mRNA surveillance pathway (Fig. S5J through O).

According to the fuzzy C-means clustering algorithm (Fig. 7L), Clusters 2, 3, 4, and 5 represent the upregulated DEGs at three timepoints, while Cluster 1 represents the downregulated DEGs at three timepoints, such as the signaling pathways ribosome (Mrpl30, Mrps9, Rpl37a) and RNA polymerase (Polr3f, Polr2b, Polr2j). The expression of genes in the Toll-like receptor signaling pathway (Ly96, Stat1, Tlr5) was consistently upregulated at 3, 5, and 7 days (Cluster 2), while the expression of genes in the PPAR signaling pathway (Acadl, Dbi, Rxrg) was persistently upregulated at 5 and 7 days (Cluster

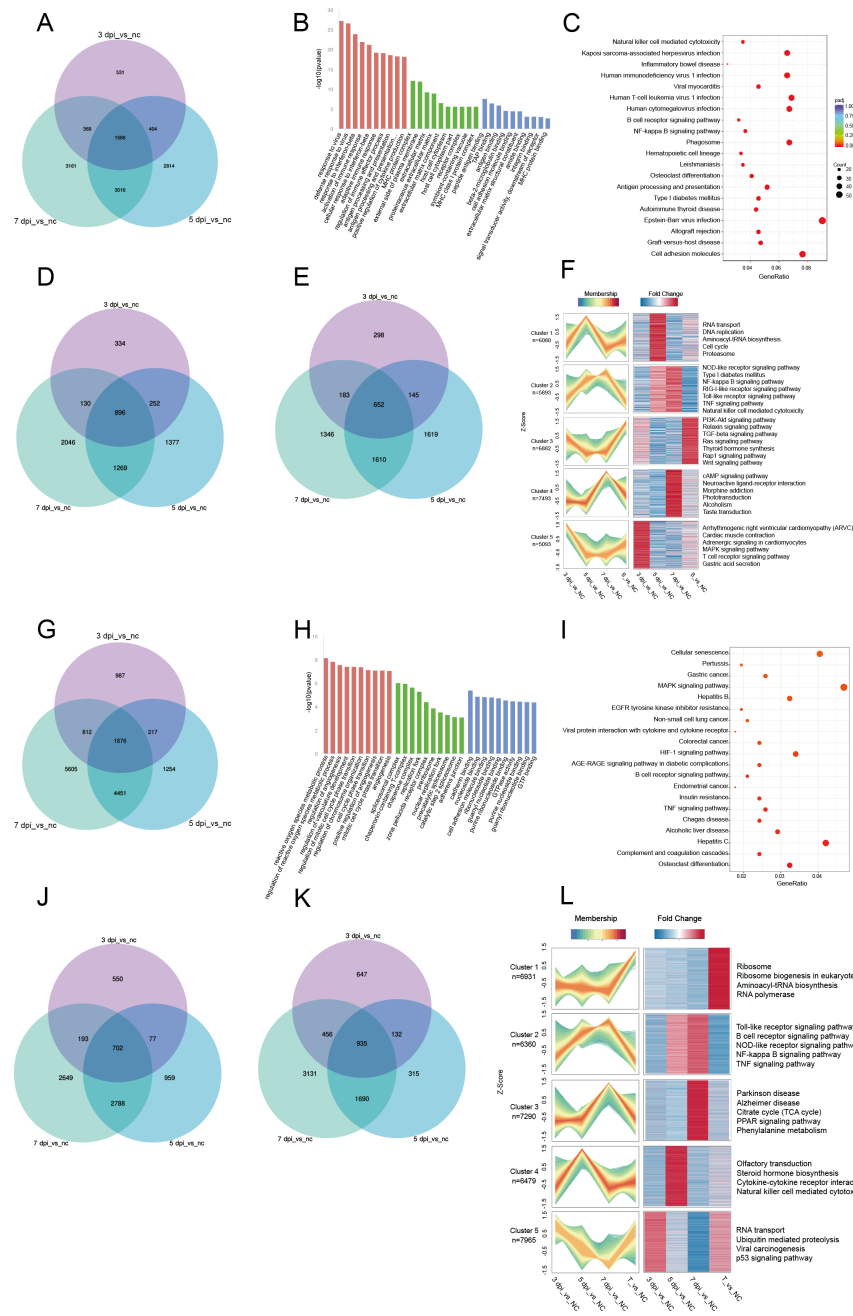


FIG 7 Dynamic of gene expression profiles in mouse spleen and thymus after CA6 infection. (A) Venn diagram of common DEGs at different timepoints. (B) GO analysis of common DEGs (A). (C) KEGG analysis of common DEGs (A). (D and E) Venn diagram of commonly upregulated (D) and downregulated (E). (F) Fuzzy C-means clustering of spleen at 3, 5, and 7 dpi, respectively. (G) Venn diagram of common DEGs at different timepoints. (H) GO analysis of common DEGs (G). (I) KEGG analysis of common DEGs (G). (J and K) Venn diagram of commonly upregulated (J) and downregulated (K). (L) Fuzzy C-means clustering of thymus at 3, 5, and 7 dpi, respectively. The values of S_vs_NC and T_vs_NC are set to 1.

3). Conversely, the expression of genes involved in olfactory transduction (Olfr1415, Olfr1408, Olfr433) and NK cell-mediated cytotoxicity (Zap70, Cd244a, Vav2) reached its peak at 5 days (Cluster 4). In contrast, only genes related to the p53 signaling pathway (Cop1, Ddb2, Bcl2l1) were upregulated at 3 days (Cluster 5).

Histopathological changes in other organs

In addition to skeletal muscle and brain, histological changes in other tissues of infected mice were observed (Fig. 8). In cardiac tissue, there was a slight amount of myocardial fiber necrosis and calcification, mild hydropic degeneration of a small proportion of myocardial fibers, and a loosely stained cytoplasm. In liver tissue, relatively large areas of extramedullary hematopoietic foci were observed within the liver sinusoids, along with infrequent multinucleated giant cells and modest infiltration of neutrophils around the portal area of bile ducts. Localized venous congestion and dilation were observed. In lung tissue, there was an increased thickness of alveolar walls and mild infiltration of neutrophils on the alveolar walls. Stomach tissue showed significant dilation with abundant luminal content, thinning of the mucosal layer, slight epithelial cell degeneration, and the presence of circular vacuoles in the cytoplasm. Small intestine tissue exhibited a reduced number of goblet cells, with mild lymphocyte infiltration at the base

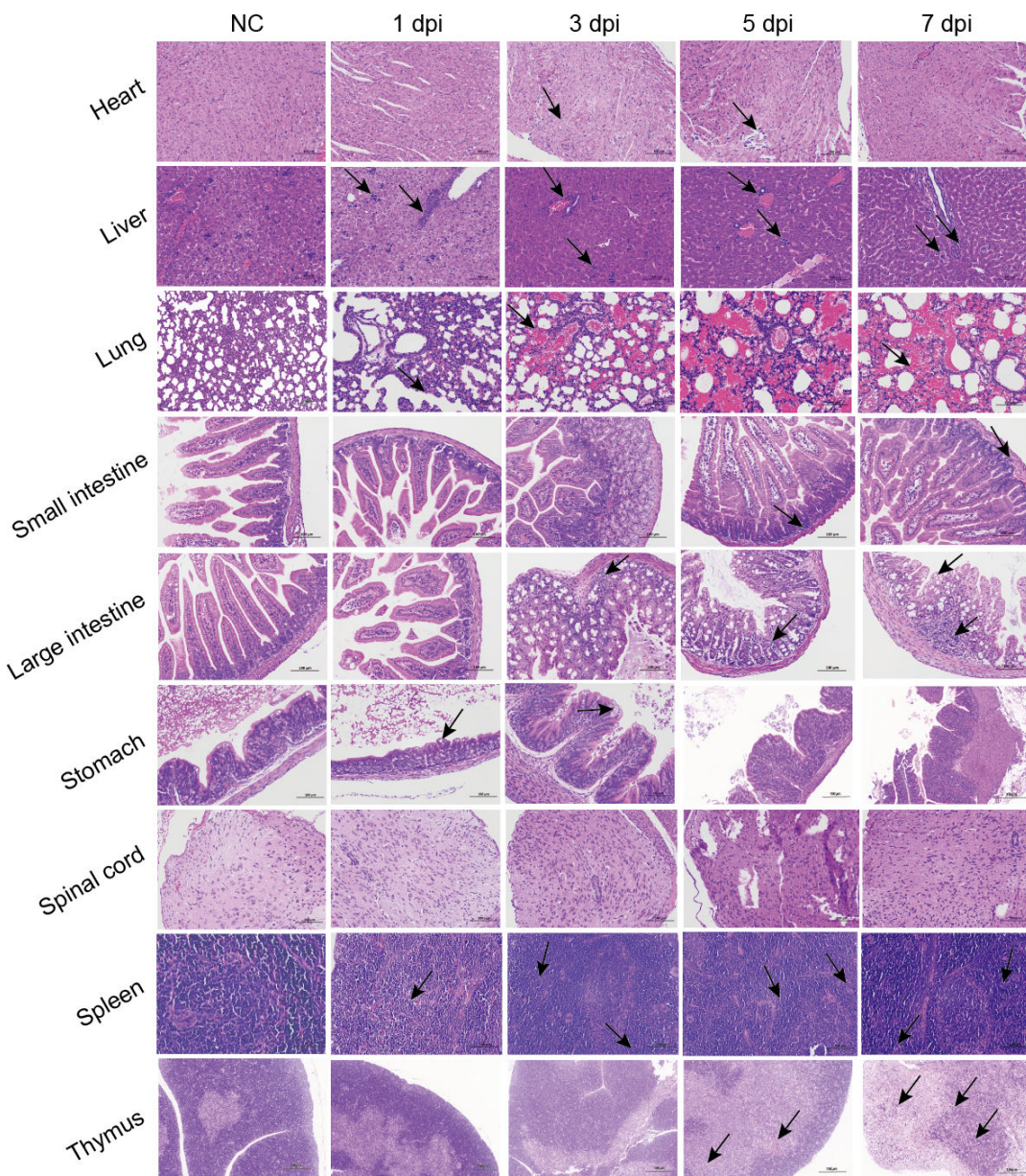


FIG 8 Pathological changes in the heart, lungs, stomach, large intestine, small intestine, liver, and spinal cord of mice infected with CA6 virus at 1, 3, 5, and 7 dpi. 200 \times . The arrows represent typical lesion sites.

of the mucosal layer. In the large intestine, a small amount of epithelial cell necrosis and shedding in the mucosal layer was observed, along with deep-stained pyknotic nuclei, reduced goblet cell count, slight expansion of many intestinal glands, presence of a few inflammatory cells within the intestinal glands, and mild lymphocyte infiltration in the mucosal layer. No significant lesions were observed in the spinal cord. The spleen tissue showed reduced white pulp content, with the disappearance of abundant white pulp structures; the red pulp exhibited extensive infiltration of neutrophils and frequent presence of multinucleated macrophages. The thymic tissue exhibited a small amount of cell necrosis in the cortex, characterized by nuclear condensation and fragmentation, while localized mild hemorrhage was observed in the medulla.

DISCUSSION

In recent years, there has been a rapid increase in HFMD outbreaks caused by CA6, necessitating the need for alternative animal models. Neonatal mice have been used as models for various enterovirus infections to study their pathogenesis processes (21, 23, 24). However, existing mouse models for CA6 have several limitations, including the route of infection, mouse-adapted strains used, and the specific virus strain used (20). Intragastric inoculation closely mimics the natural infection route, making it more relevant and suitable for simulating the progression of the disease in humans. The strain we utilized was a clinical isolate, further ensuring the rigor of the study. This model demonstrated similar outcomes to other models in terms of weight loss, hind limb paralysis, viral replication in muscles, induction of inflammation, infiltration of inflammatory cells, and elevation of inflammatory cytokines. Compared to clinical reports and EV71-infected patients and models, CA6-infected mice did not exhibit brain lesions; however, viral replication was detected in the brain. Additionally, RNA sequencing of blood, muscle, brain, spleen, and thymus tissues revealed that the brain had the most significant gene expression abnormalities. This suggests that viral replication induced anomalies in the brain. The ongoing escalation of viral presence in the spinal cord indicates viral invasion of the nervous system, suggesting that the virus spreads from the spinal cord to the brain. This study cannot exclude the possibility that the viral nucleic acids detected in various tissues are a result of viremia rather than actual viral replication within the tissues. However, the findings in the nervous system, particularly in the spinal cord, enhance our confidence in the neurotropism of the virus. First, the significantly higher viral copy numbers in the spinal cord compared to the blood indicate that mere systemic viral dissemination cannot explain the presence of viral concentrations within neural tissues exceeding those in the blood. Second, the substantially higher viral copy numbers in the spinal cord at 7 dpi compared to 5 dpi, while the blood showed lower viral copy numbers at 7 dpi compared to 5 dpi, suggesting distinct dynamics of viral copy numbers between the two regions. These conflicting viral copy number trends imply the possibility of viral invasion and replication within the spinal cord. Thus, the spinal cord might serve as an "umbilical cord" for CA6 virus invasion into brain tissue, consistent with previous studies on other enteric viruses (25).

Furthermore, the inflammatory characteristics in the spinal cord differ from those in muscles, featuring a specific infiltration of neutrophils, which distinguishes it from other CA6 models (22). Flow cytometry analysis revealed an elevated proportion of neutrophils and monocytes in the peripheral blood after infection, indicating an activated immune response against CA6 invasion. Post infection, there was a significant increase in the overall serum levels of the proinflammatory cytokines IL-6, IL-18, TNF- α , and IFN- γ . Growing amounts of evidence suggest an association between abnormal cytokine levels and central nervous system complications caused by EV71 and CA16 infections (26, 27). Our findings indicated the production of cytokines and inflammatory cells (neutrophils and monocytes) in the blood of CA6-infected mice. In addition, hemorrhage and edema in lung tissues after infection may accelerate mouse mortality. This observation is consistent with cases of fatal outcomes in severe clinical cases due to pulmonary edema (28).

The commonality of differentially expressed genes detected through RNA sequencing across various tissues parallels that of the majority of infectious disease patients and models. Inflammation and immune-related pathways are activated, including immune signals such as NOD, Toll, RIG-1, and NF- κ B, which transmit from the external environment to receptors, the cytoplasm, and the cell nucleus, thereby triggering the entire process of inflammation. Implicated genes include Rnasel, Stat1, and Casp8, which are also activated in other infectious diseases, such as SARS-CoV-2 (29), variola virus (30), and HIV-1 (31).

We observed downregulated genes of interest, and in the context of pathogenic infections, the downregulation of host genes often signifies the hijacking of the host by the virus, thereby facilitating viral synthesis, suppressing the host immune response, and consequently promoting viral replication (32). GO and KEGG analyses revealed that genes associated with T-cell and antibody generation pathways were downregulated in peripheral blood. Fuzzy-C analysis indicated that in muscles, the gene expression related to T-cell and antibody generation pathways only initiated activation in the later stages of infection. The host's specific immune response was inhibited or delayed. In the brain and muscle tissues, downregulated genes are mainly enriched in the mTOR signaling pathway, including genes such as Fzd7 (33), which is primarily involved in cell proliferation, growth, autophagy regulation, and immune modulation. Additionally, in muscle tissue, the PI3K-Akt signaling pathway is downregulated, encompassing genes such as Ppp2r5a (34), primarily associated with immune regulation, T-cell activation, and differentiation, indicating the emergence of an immune-suppressive response following CA6 infection. Thymic tissue is related to osteoblast differentiation, complement and coagulation cascades, and the TNF signaling pathway, while splenic tissue is associated with various viral infections, NK cell-mediated cytotoxicity, and antigen processing and presentation pathways. These findings underscore alterations in DEGs within multiple immune-related signaling pathways across various tissues, highlighting the significant impact of viral infection on the immune system.

Post infection, whether in blood, muscles, brain, or thymus, GO and KEGG analyses consistently revealed upregulation of genes associated with cellular respiration, oxidative phosphorylation, ATP metabolism, and cell division. Furthermore, Fuzzy-C analysis indicated that these signaling pathways were upregulated in the early stages of infection. These findings signify enhanced energy metabolism and cell division, yet intriguingly, we observed no increase in mouse body weight. This observation might imply that energy and cellular reproduction are primarily channeled toward inflammatory cells. This suggests that in growing animals encountering infection, an internal regulatory system may redirect energy toward inflammation while temporarily pausing growth and development. Moreover, this phenomenon is conceivably intertwined with the regulation of inflammatory responses, as cells mobilize resources toward mounting an effective defense against the infective agent. In the broader context of infectious diseases, the similar dampening of these intricate signaling pathways has been linked to the orchestration of inflammatory and immune responses, reshaping cellular metabolic dynamics, and the virus's strategic exploitation of the host cell's resources for its own replication endeavors (35). Interestingly, in the blood, genes related to autophagy (such as Atg9a) were also downregulated. Autophagy plays a role in providing energy and nutrients to cells, aiding in maintaining metabolic balance. Under conditions of cellular starvation or stress, autophagy can breakdown organic materials within cells, supplying essential nutrients to support cell growth and survival (36).

We identified upregulation of certain genes specific to other diseases. RNA-seq results revealed gene expression patterns resembling those seen in the brain tissue of patients with Parkinson's disease, suggesting potential pathogenic gene expression. For instance, the upregulation of Cox5b, specific to Parkinson's disease, was observed. While CA6 infection has not been reported to cause Parkinson's disease, it does lead to neuronal loss similar to that seen in patients with Parkinson's disease. Despite the absence of apparent brain pathology, this suggests that the molecular basis for the lesion already

exists. Furthermore, genes associated with inflammatory bowel disease were found to be upregulated. CA6 is a gastrointestinal virus, and while CA6 infection rarely results in clinical IBD, we detected CA6 replication in the small intestine after oral infection. This led to irregular villous arrangement and limited lymphocyte infiltration in the mucosal layer of the small intestine. Correspondingly, diarrhea was observed in infected mice, which warrants our attention to whether IBD might be a latent manifestation and its potential clinical risks triggered by CA6 infection.

When exploring the characteristics of CA6 infection, it is notable to compare it with other major causative agents of HFMD such as EV71 and CA16. Clinical infection with each of three viruses will lead to typical manifestations of HFMD including fever, vesicular rash on the hands, feet, and buttocks, and oral mucosal ulcers, while merely EV71 infection was associated with severe neurological complications of HFMD. In mice model, the three viruses also share many similar demonstrations, such as mainly replicating in skeletal muscle, disseminating into other organs by viremia, and necrotizing myositis as the most severe histopathological injuries among all the organs. In terms of the nervous system, infection with a lethal dose of CA6 in mice did not result in significant brain lesions, whereas infection with a lethal dose of EV71 led to pronounced vascular congestion, hemorrhage, and inflammatory cell infiltration in the brainstem perivascular areas (37). This difference may explain the relatively mild clinical symptoms observed in CA6 infection (38). After CA6 infection in mice, an upregulation of genes associated with Parkinson's disease and inflammatory bowel disease has been detected. In contrast, studies indicate that following infections with EV71 and CA16, the most significantly enriched pathway, as revealed by KEGG pathway analysis, is associated with herpes simplex virus (27). These differences highlighted potential variations in the pathology and immunology among different HFMD viruses, providing clues for further understanding of the pathology of these viral infections.

Above all, we established a CA6 mouse infection model using oral administration, mimicking natural infection. This model shows viral pathogenicity, tissue distribution, and pathology resembling clinical symptoms. It innovates on previous injection models, aiding virus research and drug development.

MATERIALS AND METHODS

Viruses

In this experiment, clinical isolates of CA6 (ATCC VR-1801) were used and stored. All viral strains were preserved at -80°C .

Mouse experiments

Seven-day-old specific pathogen-free (SPF) BALB/c mice weighing 6–8 g were purchased from SPF (Beijing) Biotechnology Co., Ltd. The mice were housed in individual ventilated cages with sterile water and sterile mouse feed provided *ad libitum*.

For infection, the virus was diluted to three different concentrations: $1 \times 10^{7.5}$ TCID₅₀/mL, $1 \times 10^{6.5}$ TCID₅₀/mL, and $1 \times 10^{5.5}$ TCID₅₀/mL, and then mice were orally administered with 100 μL of virus solution (inoculation dose for each mouse was $1 \times 10^{6.5}$ TCID₅₀, $1 \times 10^{5.5}$ TCID₅₀, or $1 \times 10^{4.5}$ TCID₅₀, respectively) using a gavage needle [plastic feeding tubes, 22 ga (black) \times 25 mm]. When administered orally at a dose of $1 \times 10^{6.5}$ TCID₅₀, the survival rate of mice was 0%. Therefore, we chose this dose for subsequent model creation experiments. Typically, 8–10 mice were used for administration of each dose during viral challenge. The mice were observed for symptoms such as weight loss and disease manifestations, and the symptoms were recorded daily. The muscles involved in present experiment were collected from hind limbs of infected mice.

RNA extraction and quantitative real-time PCR

RNA was extracted from mouse blood and other tissues using TRIzol reagent (Invitrogen, Carlsbad, CA, USA). cDNA was obtained by reverse transcription with a RevertAid First Strand cDNA Synthesis Kit (Thermo Fisher, USA). Quantitative real-time PCR was performed using a QuantiTect Probe RT-PCR Kit (Qiagen, Germany) according to the manufacturer's instructions. The standard curve was generated by a series of 10-fold dilutions of a recombinant plasmid of known concentration. The primer sequences were as follows: TCA6-F (5'-GCCCTGAATCGGGCTAACCTAA-3'), TCA6-R (5'-CGGACACCCAAA GTAGTCGGTTCC-3'), and CA6-TaqProbe (FAM- CCATTACGACGCACCACCCCTGGATTGA - BHQ1).

Pathological examination

Different tissues of infected mice were collected and fixed in 10% formalin for 72 h, dehydrated with gradient alcohol, and embedded in paraffin. Paraffin sections of the tissues (5 µm thick) were stained with hematoxylin and eosin to identify histopathological changes in the organs, such as cell damage and inflammatory cell infiltration.

Flow cytometry analysis

Flow cytometry analysis was performed on peripheral blood samples. Briefly, the blood samples were added to centrifuge tubes containing red blood cell lysis buffer (such as ammonium-chloride-potassium solution) and incubated at 4°C in the dark for 5–10 min. Subsequently, the samples were washed with PBS buffer before flow cytometry analysis.

For cell selection, specific antibodies were used for labeling. CD45 was used to select leukocytes, CD11B for myeloid cells, LY6G for neutrophils, LY6C for monocytes, and F4/80 for macrophages. The appropriate antibodies and fluorophores used included CD45-APC, CD11B-APC-CY7, LY6G-BV421, LY6C-PECY7, and F4/80-PE. The gating strategy is founded on CD45⁺, CD11B⁺ gating, where LY6G⁺LY6C⁺ is designated as the neutrophil population, and LY6G⁻LY6C⁺ is designated as the monocyte population.

Immunohistochemical staining

Paraffin sections (5 µm thickness) of muscle and spinal cord were deparaffinized three times in xylene for 10 min, followed by hydration in an ethanol gradient (100%, 95%, 80%, and 70%). Antigen retrieval was performed by heating the sections in 0.01 M citrate buffer, and endogenous peroxidases in the sections were quenched for 10 min. After blocking in 10% goat serum for 1 h, the sections were incubated with anti-MAC-2 (Cedarlane Laboratories, CL8942AP, the dilution ratio was 1:1,000) and anti-LY6G (Abcam, ab238132, dilution ratio was 1:2,000) monoclonal antibodies at 4°C overnight. Subsequently, the sections were incubated with HRP-labeled goat anti-rat/rabbit IgG secondary antibodies. The samples were then visualized using 3,3'-diaminobenzidine tetrahydrochloride and counterstained with hematoxylin. Finally, the sections were observed under a light microscope.

Confocal microscopy

Paraffin sections of muscle and spinal cord were deparaffinized in xylene, hydrated in ethanol, thermally repaired in alkaline antigenic repair solution, and cooled to room temperature. Sections were then blocked in 10% goat serum for 10 min and stained with an anti-MAC-2 monoclonal antibody (1:500 dilution) at room temperature for 1 h. After incubation with HRP-labeled goat anti-rat IgG secondary antibody for 10 min, the sections were stained with PPD520. The above steps were repeated to stain with the following antibodies: LY6G (the dilution ratio was 1:1,000) and VP1 (the dilution ratio was 1:500), using goat anti-rabbit IgG as the secondary antibody. PPD570 and PPD650 were used to express the fluorescent signal. For DNA detection, DAPI was used. Sections were observed via fluorescence microscopy.

Luminex

Serum was collected at different timepoints postinfection for cytokine detection. The concentrations of cytokines were measured using a Cytokine & Chemokine 14-Plex Porcine Panel (Thermo Fisher, USA) with a Luminex 200 according to the manufacturer's instructions.

RNA sequencing

RNA-seq and bioinformatic analysis were performed and analyzed by Beijing Nuohe Zhiyuan Technology Ltd. First, RNA was extracted and qualified, and a common eukaryotic transcriptome library was constructed by the magnetic bead enrichment method. A Qubit 2.0 was used for the initial quantification of the library. An Agilent 2100 was used for insert size detection, and qRT-PCR was used to detect the effective concentration of the library. An Illumina PE150 was applied for sequencing according to the effective concentration and data output of the library. The basic principle was sequencing at the same time as synthesis. Bioinformatic analysis comprised comparison with HISAT2, quantitative analysis with HTSeq, differential expression analysis with DESeq2, and functional enrichment with KEGG analysis and fuzzy C-means algorithm analysis. Genes with $|fold\ change\ (FC)| > 2$ and $P < 0.05$ were defined as differentially expressed genes. KEGG pathway enrichment analysis was separately performed for the DEGs with altered expression in each organ, including both upregulated and downregulated DEGs. The top 10 pathways with the highest enrichment levels (lowest P value) in each organ were selected and integrated into bubble plots.

The purpose of VENN analysis is to illustrate the overlap and uniqueness of DEGs at different timepoints, aiding in understanding the relationships and significance of gene sets. GO analysis was used to comprehend the functional characteristics of differentially expressed genes and their roles within the cell. KEGG analysis maps DEGs onto biological metabolic and signaling pathways, enabling an understanding of gene interactions and pathway involvement in biological processes. Fuzzy C-means analysis categorizes gene expression patterns into clusters with similar expression features, aiding in the discovery of shared expression patterns and gene functions.

Statistical analysis

Viral load values are expressed as the geometric mean with geometric SD, and other values are expressed as the mean \pm SEM. The statistical significance of differences in viral loads and chemokine analysis was determined using a *t* test. The false discovery rate in RNA sequencing was regulated by adjusting the P values through Benjamini and Hochberg's method. P values < 0.05 were considered statistically significant: $*P < 0.05$. Statistical analysis was performed using GraphPad Prism software version 9.

ACKNOWLEDGMENTS

We thank Peking Union Medical College for the opportunity to develop this work.

This work was supported by the National Key Research and Development Project of China (grant no. 2022YFC2303404) and the CAMS Innovation Fund for Medical Sciences (CIFMS) (grants 2022-I2M-1-020 and 2021-I2 M-035).

Conceptualization: J.N.L., B.B.Z.; Methodology: L.H.Z., W.J.P., J.W., X.H.W., N.R., G.X.Z., H.K.Y., X.Y.D.; Writing-Original Draft: L.H.Z.; Writing-Review and Editing: J.N.L.; Funding Acquisition: J.N.L.; Resources: J.N.L.; Supervision: J.N.L. All authors read and approved the final manuscript.

AUTHOR AFFILIATIONS

¹Institute of Laboratory Animal Science, Chinese Academy of Medical Sciences and Comparative Medicine Center, Peking Union Medical College, Beijing, China

²NHC Key Laboratory of Human Disease Comparative Medicine, Beijing, China

³National Center of Technology Innovation for Animal Models, Beijing, China

⁴Servicebio, Wuhan, China

AUTHOR ORCIDs

Lihong Zhang  <http://orcid.org/0000-0001-6831-360X>

Wanjun Peng  <http://orcid.org/0000-0002-8395-324X>

Binbin Zhao  <http://orcid.org/0000-0003-0214-2224>

Jiangning Liu  <http://orcid.org/0000-0002-1264-6664>

FUNDING

Funder	Grant(s)	Author(s)
MOST National Key Research and Development Program of China (NKP)	2022YFC2303404	Lihong Zhang Wanjun Peng Jing Wu Xiaohui Wei Na Rong Gengxin Zhang Hekai Yang Xiaoyue Ding Binbin Zhao Jiangning Liu
CAMS Innovation Fund for Medical Sciences	2022-I2M-1-020, 2021-I2M-035	Lihong Zhang Wanjun Peng Jing Wu Xiaohui Wei Na Rong Gengxin Zhang Hekai Yang Xiaoyue Ding Binbin Zhao Jiangning Liu

DATA AVAILABILITY

The RNA-sequencing data sets generated for this study can be found in the Gene Expression Omnibus with accession no. [GSE243200](#). Further inquiries may be directed to the corresponding author.

ETHICS APPROVAL

Mouse studies were performed in an animal biosafety level 2 (ABSL-2) facility using high-efficiency particulate air (HEPA)-filtered isolators. All animal procedures were reviewed and approved by the Institutional Animal Care and Use Committee of the Institute of Laboratory Animal Science, Peking Union Medical College (ILAS, PUMC) (LJN22008).

ADDITIONAL FILES

The following material is available [online](#).

Supplemental Material

Figure S1 (JVI01358-23-S0001.tif). Volcano plot, GO analysis, and KEGG analysis results of RNA-Seq in mouse blood after CA6 virus infection.

Figure S2 (JVI01358-23-S0002.tif). Volcano plot, GO analysis, and KEGG analysis results of RNA-Seq in mouse muscles after CA6 virus infection.

Figure S3 (JVI01358-23-S0003.tif). Volcano plot, GO analysis, and KEGG analysis results of RNA-Seq in the mouse brain after CA6 virus infection.

Figure S4 (JVI01358-23-S0004.tif). Volcano plot, GO analysis, and KEGG analysis results of RNA-Seq in the mouse spleen after CA6 virus infection.

Figure S5 (JVI01358-23-S0005.tif). Volcano plot, GO analysis, and KEGG analysis results of RNA-Seq in the mouse thymus after CA6 virus infection.

Supplemental legends (JVI01358-23-S0006.docx). Legends for Fig. S1 to S5.

REFERENCES

- Zhu B, Zhong J, Xia H, Gong S, Xiao M, Xie J, Zhang Y, Hua L, Lian G. 2010. Etiology of hand, foot and mouth disease in Guangzhou in 2008. *Zhonghua Er Ke Za Zhi= Chinese Journal of Pediatrics* 48:127–130.
- Ryu WS, Kang B, Hong J, Hwang S, Kim A, Kim J, Cheon D-S. 2010. Enterovirus 71 infection with central nervous system involvement, South Korea. *Emerg Infect Dis* 16:1764–1766. <https://doi.org/10.3201/eid1611.100104>
- Cox B, Levent F. 2018. Hand, foot, and mouth disease. *JAMA* 320:2492. <https://doi.org/10.1001/jama.2018.17288>
- Wang Y, Feng Z, Yang Y, Self S, Gao Y, Longini IM, Wakefield J, Zhang J, Wang L, Chen X, et al. 2011. Hand, foot, and mouth disease in China: patterns of spread and transmissibility. *Epidemiology* 22:781–792. <https://doi.org/10.1097/EDE.0b013e318231d67a>
- Aswathyraj S, Arunkumar G, Alidjinou EK, Hober D. 2016. Hand, foot and mouth disease (HFMD): emerging epidemiology and the need for a vaccine strategy. *Med Microbiol Immunol* 205:397–407. <https://doi.org/10.1007/s00430-016-0465-y>
- Fujimoto T, Iizuka S, Enomoto M, Abe K, Yamashita K, Hanaoka N, Okabe N, Yoshida H, Yasui Y, Kobayashi M, et al. 2012. Hand, foot, and mouth disease caused by coxsackievirus A6. *Emerg Infect Dis* 18:337–339. <https://doi.org/10.3201/eid1802.111147>
- Bian L, Wang Y, Yao X, Mao Q, Xu M, Liang Z. 2015. Coxsackievirus A6: a new emerging pathogen causing hand, foot and mouth disease outbreaks worldwide. *Expert Rev Anti Infect Ther* 13:1061–1071. <https://doi.org/10.1586/14787210.2015.1058156>
- Xiaoling ZYH. 2016. Research progress on hand, foot and mouth disease caused by coxsackievirus A6. *Med Rec* 2016:3953–3956.
- Blomqvist S, Klemola P, Kaijalainen S, Paananen A, Simonen M-L, Vuorinen T, Roivainen M. 2010. Co-circulation of coxsackieviruses A6 and A10 in hand, foot and mouth disease outbreak in Finland. *J Clin Virol* 48:49–54. <https://doi.org/10.1016/j.jcv.2010.02.002>
- Osterback R, Vuorinen T, Linna M, Susi P, Hyypia T, Waris M. 2009. Coxsackievirus A6 and hand, foot, and mouth disease, Finland. *Emerg Infect Dis* 15:1485–1488. <https://doi.org/10.3201/eid1509.090438>
- Mirand A, Henquell C, Archimbaud C, Ughetto S, Antona D, Bailly J-L, Peigue-Lafeuille H. 2012. Outbreak of hand, foot and mouth disease/herpangina associated with coxsackievirus A6 and A10 infections in 2010, France: a large citywide, prospective observational study. *Clin Microbiol Infect* 18:E110–E118. <https://doi.org/10.1111/j.1469-0691.2012.03789.x>
- Wei S-H, Huang Y-P, Liu M-C, Tsou T-P, Lin H-C, Lin T-L, Tsai C-Y, Chao Y-N, Chang L-Y, Hsu C-M. 2011. An outbreak of coxsackievirus A6 hand, foot, and mouth disease associated with onychomadesis in Taiwan, 2010. *BMC Infect Dis* 11:346. <https://doi.org/10.1186/1471-2334-11-346>
- Flett K, Youngster I, Huang J, McAdam A, Sandora TJ, Rennick M, Smole S, Rogers SL, Nix WA, Oberste MS, Gellis S, Ahmed AA. 2012. Hand, foot, and mouth disease caused by coxsackievirus A6. *Emerg Infect Dis* 18:1702–1704. <https://doi.org/10.3201/eid1810.120813>
- Centers for Disease, C. and Prevention. 2012. Notes from the field: severe hand, foot, and mouth disease associated with coxsackievirus A6 — Alabama, Connecticut, California, and Nevada, November 2011–February 2012. *MMWR Morb Mortal Wkly Rep* 61:213–214.
- Guimbao J, Rodrigo P, Alberto MJ, Omeñaca M. 2010. Onychomadesis outbreak linked to hand, foot, and mouth disease. *Euro Surveill* 15:37. <https://doi.org/10.2807/ese.15.37.19663-en>
- Huang W-C, Huang L-M, Lu C-Y, Cheng A-L, Chang L-Y. 2013. Atypical hand-foot-mouth disease in children: a hospital-based prospective cohort study. *Virol J* 10:209. <https://doi.org/10.1186/1743-422X-10-209>
- Rao CD, Yergolkar P, Shankarappa KS. 2012. Antigenic diversity of enteroviruses associated with nonpolio acute flaccid paralysis, India, 2007–2009. *Emerg Infect Dis* 18:1833–1840. <https://doi.org/10.3201/eid1811.111457>
- Wang J, Cao Z, Zeng DD, Wang Q, Wang X, Qian H. 2014. Epidemiological analysis, detection, and comparison of space-time patterns of Beijing hand-foot-mouth disease (2008–2012). *PLoS ONE* 9:e92745. <https://doi.org/10.1371/journal.pone.0092745>
- Yang L, Mao Q, Li S, Gao F, Zhao H, Liu Y, Wan J, Ye X, Xia N, Cheng T, Liang Z. 2016. A neonatal mouse model for the evaluation of antibodies and vaccines against coxsackievirus A6. *Antiviral Res* 134:50–57. <https://doi.org/10.1016/j.antiviral.2016.08.025>
- Zhang Z, Dong Z, Wei Q, Carr MJ, Li J, Ding S, Tong Y, Li D, Shi W. 2017. A neonatal murine model of coxsackievirus A6 infection for evaluation of antiviral and vaccine efficacy. *J Virol* 91. <https://doi.org/10.1128/JVI.02450-16>
- Jiang Z, Zhang Y, Lin H, Cheng Q, Lu X, Liu W, Zhou R, Zhong B, Tian X. 2021. A 10-day-old murine model of coxsackievirus A6 infection for the evaluation of vaccines and antiviral drugs. *Front Immunol* 12:665197. <https://doi.org/10.3389/fimmu.2021.665197>
- Li D, Sun T, Tao L, Ji W, Zhu P, Liang R, Zhang Y, Chen S, Yang H, Jin Y, et al. 2022. A mouse-adapted CVA6 strain exhibits neurotropism and triggers systemic manifestations in a novel murine model. *Emerg Microbes Infect* 11:2248–2263. <https://doi.org/10.1080/22221751.2022.2119166>
- Lee S-Y, Ko M-K, Lee K-N, Choi J-H, You S-H, Pyo H-M, Lee M-H, Kim B, Lee J-S, Park J-H. 2016. Application of mouse model for effective evaluation of foot-and-mouth disease vaccine. *Vaccine* 34:3731–3737. <https://doi.org/10.1016/j.vaccine.2016.06.008>
- Mao Q, Wang Y, Gao R, Shao J, Yao X, Lang S, Wang C, Mao P, Liang Z, Wang J. 2012. A neonatal mouse model of coxsackievirus A16 for vaccine evaluation. *J Virol* 86:11967–11976. <https://doi.org/10.1128/JVI.00902-12>
- Khong WX, Yan B, Yeo H, Tan EL, Lee JJ, Ng JKW, Chow VT, Alonso S. 2012. A non-mouse-adapted enterovirus 71 (EV71) strain exhibits neurotropism, causing neurological manifestations in a novel mouse model of EV71 infection. *J Virol* 86:2121–2131. <https://doi.org/10.1128/JVI.06103-11>
- Wang S-M, Lei H-Y, Liu C-C. 2012. Cytokine immunopathogenesis of enterovirus 71 brain stem encephalitis. *Clin Dev Immunol* 2012:876241. <https://doi.org/10.1155/2012/876241>
- Sun Y-S, Yang Z-N, Xu F, Chen C, Lu H-J, Jiang J-M, Zhang Y-J, Zhu H-P, Yao P-P. 2019. Global gene expression analysis of the brainstem in EV71- and CVA16-infected gerbils. *Viruses* 12. <https://doi.org/10.3390/v12010046>

28. Sun T, Li D, Dai X, Meng C, Li Y, Cheng C, Ji W, Zhu P, Chen S, Yang H, et al. 2023. Local immune dysregulation and subsequent inflammatory response contribute to pulmonary edema caused by *Enterovirus* infection in mice. *J Med Virol* 95:e28454. <https://doi.org/10.1002/jmv.28454>
29. Lee D, Le Pen J, Yatim A, Dong B, Aquino Y, Ogishi M, Pescarmona R, Talouarn E, Rinchai D, Zhang P, et al. 2023. Inborn errors of OAS-RNase L in SARS-CoV-2-related multisystem inflammatory syndrome in children. *Science* 379:eab03627. <https://doi.org/10.1126/science.abo3627>
30. Talbot-Cooper C, Pantalejevs T, Shannon JP, Cherry CR, Au MT, Hyvönen M, Hickman HD, Smith GL. 2022. Poxviruses and paramyxoviruses use a conserved mechanism of STAT1 antagonism to inhibit interferon signaling. *Cell Host Microbe* 30:357–372. <https://doi.org/10.1016/j.chom.2022.01.014>
31. Wan L-Y, Huang H-H, Zhen C, Chen S-Y, Song B, Cao W-J, Shen L-L, Zhou M-J, Zhang X-C, Xu R, et al. 2023. Distinct inflammation-related proteins associated with T cell immune recovery during chronic HIV-1 infection. *Emerg Microbes Infect* 12:2150566. <https://doi.org/10.1080/2221751.2022.2150566>
32. Lv C, Zhang Q, Zhao L, Yang J, Zou Z, Zhao Y, Li C, Sun X, Lin X, Jin M. 2022. African swine fever virus infection activates inflammatory responses through downregulation of the anti-inflammatory molecule C1QTNF3. *Front Immunol* 13:1002616. <https://doi.org/10.3389/fimmu.2022.1002616>
33. Chen Q, Wang H, Li Z, Li F, Liang L, Zou Y, Shen H, Li J, Xia Y, Cheng Z, et al. 2022. Circular RNA ACTN4 promotes intrahepatic cholangiocarcinoma progression by recruiting YBX1 to initiate FZD7 transcription. *J Hepatol* 76:135–147. <https://doi.org/10.1016/j.jhep.2021.08.027>
34. Leonard D, Huang W, Izadmehr S, O'Connor CM, Wiredja DD, Wang Z, Zaware N, Chen Y, Schlatzer DM, Kisela J, et al. 2020. Selective PP2A enhancement through biased heterotrimer stabilization. *Cell* 181:688–701. <https://doi.org/10.1016/j.cell.2020.03.038>
35. Xu M, Huseinovic A, Jaspers A, Yuan L, Steenbergen RDM. 2023. Downregulation of miR-193a/b-3p during HPV-induced cervical carcinogenesis contributes to anchorage-independent growth through PI3K–AKT pathway regulators. *J Med Virol* 95:e28589. <https://doi.org/10.1002/jmv.28589>
36. Mizushima N, Komatsu M. 2011. Autophagy: renovation of cells and tissues. *Cell* 147:728–741. <https://doi.org/10.1016/j.cell.2011.10.026>
37. Cui G, Wang H, Yang C, Zhou X, Wang J, Wang T, Ma T. 2022. Berberine prevents lethal EV71 neurological infection in newborn mice. *Front Pharmacol* 13:1027566. <https://doi.org/10.3389/fphar.2022.1027566>
38. Wu Y, Yeo A, Phoon MC, Tan EL, Poh CL, Quak SH, Chow VTK. 2010. The largest outbreak of hand; foot and mouth disease in Singapore in 2008: the role of enterovirus 71 and coxsackievirus A strains. *Int J Infect Dis* 14:e1076–e1081. <https://doi.org/10.1016/j.ijid.2010.07.006>